Three-dimensional Analytical Model for Axial-Flux Eddy-Current Couplings and Brakes under Steady-State Conditions

Thierry Lubin, Abderrezak Rezzoug

Three-dimensional Analytical Model for Axial-Flux Eddy-Current Couplings and Brakes under Steady-State Conditions

Thierry Lubin and Abderrezak Rezzoug

Université de Lorraine, Groupe de Recherche en Electrotechnique et Electronique de Nancy, GREEN, F-54500 Vandœuvre-lès-Nancy, France

This paper presents a three-dimensional (3-D) analytical model for axial-flux eddy-current couplings and brakes, leading to closed-form expressions for the torque and the axial force. The proposed model is valid under steady-state condition (constant speed operation). It takes into account the reaction field due to induced currents in the moving conducting part. In order to simplify the analysis, we adopt the assumption of linearization at the mean radius, the problem is then solved in 3-D Cartesian coordinates (curvature effects are neglected). The solution is obtained by solving the Maxwell equations with a magnetic scalar potential formulation in the non conductive regions (magnets, air-gap), and a magnetic field strength formulation in the conductive region (copper). Magnetic field distribution, axial force, and torque computed with the 3-D analytical model are compared with those obtained from 3-D finite elements simulations and experimental results.

***Index Terms*— Analytical model, Eddy-current, Moving conductor, Three-dimensional model, Torque.**

NOMENCLATURE

R_1	Inner radius of the magnets.
R_2	Outer radius of the magnets.
R_m	Mean radius of the magnets ($R_m = (R_1+R_2)/2$).
R_0	Inner radius of the copper.
R_3	Outer radius of the copper.
L	Radial length of the magnets ($L = R_2 - R_1$).
H	Radial length of the copper ($H = R_3 - R_0$).
a	Thickness of the back-iron (magnets side).
b	Magnets thickness.
c	Air-gap thickness.
d	Copper thickness.
e	Thickness of the back-iron (copper side)
α	Permanent magnets (PMs) pole-arc to pole-pitch ratio
p	Pole-pairs number.
B_r	Remanence of the PMs.
σ	Conductivity of the conducting plate (copper).
τ	Pole pitch ($\tau = R_m\pi/p$).

I. INTRODUCTION

EDDY current couplings can be used in many industrial applications such as blowers, conveyors or pumps . They can transmit a torque between a motor and a driven load without any physical contact. Compared to traditional mechanical couplings, they offer substantial advantages such as reduce maintenance, soft starting, vibrations limitation, natural protection against overload, and great tolerance to shaft misalignment [1]-[7].

Fig. 1 shows the axial-flux eddy-current coupling under consideration. It consists of two facing discs, one equipped with rare-earth PMs of alternating polarity, glued on a soft-magnetic yoke (the PMs are magnetized in the axial direction). The other disc is equipped with a conducting plate (generally copper) fixed on iron. The torque-speed curve of such devices is related to the induced currents in the conducting plate. The value and the distribution of these currents depend on the slip speed Ω between the two discs ($\Omega = \Omega_1 - \Omega_2$). The consequence of this is the Joule losses, which are inherent to the operation of this type of magnetic coupling. The efficiency of such device is given by $\eta = 1 - s$, where s is the slip ($s = \Omega/\Omega_1$). In normal operation, the slip is relatively small and can range from 2 to 5 percent [6], [7].

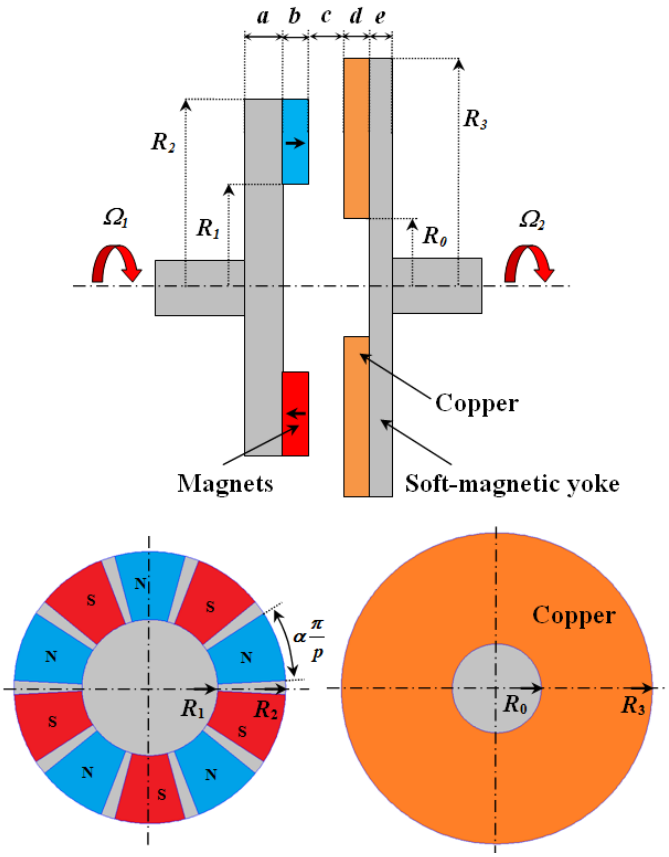

Fig. 1. Permanent-magnet axial-flux eddy-current coupling with its geometrical parameters.

Manuscript received March 25, 2015. Corresponding author: T. Lubin (e-mail: thierry.lubin@univ-lorraine.fr).

Digital Object Identifier inserted by IEEE

Analysis and design of eddy-current couplings and brakes can be achieved with analytical or numerical methods. Numerical approaches, such as finite-element method [8]-[13], give accurate results considering geometric details and nonlinearity of magnetic materials. However, they are computation time consuming and poorly flexible for the first step of design procedure especially when a 3-D analysis is required, as it is for the studied device. Analytical approaches are based on some assumptions such as simplified geometries and linear magnetic behavior. However, they present the main advantage to be quick in term of computational time. They are well suited to investigate rapidly the influence of the design parameters and during optimization procedure.

Analytical models for eddy-current couplings and brakes are usually based on 2-D approximations (i.e. mean radius model and infinite depth) [14]-[21]. The induced currents in the moving conducting plate are computed by solving the 2-D diffusion equation. The 3-D edge effects, which cannot be neglected for such devices, are usually taken into account by using an effective correction factor [22]. The method of images can also be used in order to take into account the finite boundaries of the conducting plate and the predictions are greatly improved [23]-[24]. Recently, a 3-D analytical model has been developed to compute the torque for a magnetic rotor moving above a conducting plate [25] by using the second-order vector potential approach [26]. Overall, most of the 3-D magnetic field problems that have been recently solved by an analytical way are most often dedicated to the magnetostatic case [27]-[30], and very little attention is given to 3-D eddy-current problems with moving conductors.

In this paper, we propose a fully 3-D analytical model to predict the induced currents distribution in axial-flux eddy current couplings and brakes. The proposed model is valid under steady-state condition (constant slip speed). It takes into account the reaction field due to induced currents in the moving conducting plate. The solution is obtained by solving the Maxwell equations in 3-D Cartesian coordinates by the separation of variables method (curvature effects are neglected). By using the Maxwell stress tensor, new closed-form expressions for the torque and the axial force are given. In order to show the accuracy of the proposed model, the results are compared with those obtained from 3-D finite-element simulations and experimental results.

II. Modeling Assumptions

As shown in Fig. 1, axial-flux eddy-current coupling is an inherent 3-D geometry from the modeling point of view. Indeed, the edge effects in the radial direction have a great importance on the torque-speed curve prediction and cannot be neglected [19]-[20]. As the axial-flux coupling presents a cylindrical geometry, the natural way to solve this problem is to use a cylindrical coordinate system (r, θ, z). However, this choice leads to complex partial differential equations to solve, where the magnetic field components are connected to each other. In addition, special functions (Bessel functions) arise in the solution (radial dependence of the magnetic field) when solving this problem in cylindrical coordinates [27].

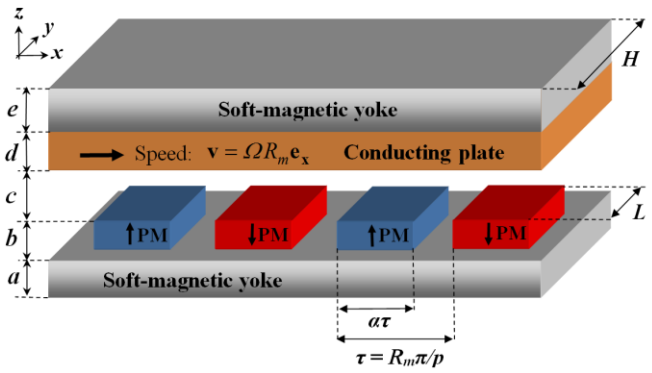

Fig. 2. 3-D representation of the equivalent linear eddy-current coupling.

It has been shown in [28] that the curvature effects in axial-flux actuators is generally a second order phenomenon and can be neglected without important errors. Therefore, the 3-D cylindrical topology of Fig. 1 can be reduced to a 3-D linear topology by using the mean radius (R_m) assumption. As shown in Fig. 2, the axial-flux eddy-current coupling is made equivalent to a linear eddy-current coupling where the x-coordinate represents the circumferential direction, the y-coordinate the radial direction, and the z-coordinate the axial direction. The system is extended to infinity in both direction along the x-axis and presents a periodicity of two pole pitch (2τ). The depth of the conducting plate and of the soft-magnetic yokes is $H = R_3 - R_0$. The depth of the magnets is $L = R_2 - R_1$ with $L < H$. In [6] and [7], it has been shown that the performances of eddy-current couplings and brakes are greatly improved if $H \simeq L + \tau$. With this condition, the induced currents in the circumferential direction (which do not contribute to the torque) are mainly located outside the useful path which corresponds to the magnet depth (see Fig. 8).

The velocity of the conducting plate $\mathbf{v}$ (m/s) is given by (1) where $\mathbf{e_x}$ is the unit vector in the x-direction.

$$\mathbf{v} = V_x \mathbf{e_x} \qquad \text{with} \qquad V_x = \Omega R_m \tag{1}$$

For simplification of the analysis, we adopt the following assumptions:

- The soft-magnetic yokes are considered with infinite magnetic permeability and zero conductivity.
- We consider only the steady state operation, i.e. constant slip speed.
- The conducting plate has a constant conductivity.
- The magnets have relative recoil permeability $\mu_r = 1$ (rare-earth PMs).

Based on the above assumptions, we neglect the induced currents in the secondary back iron (which moves with the copper), and therefore the additional braking torque. It was shown in [20] that this additional torque is small compared to the one due to the copper plate. Moreover, if the copper thickness d is well-designed (optimum value can be reach for the copper thickness [3], [6], [7]), induced currents in the iron part will be limited.

III. 3-D Analytical Model

Sectional views of the linear eddy-current coupling in planes (*x*-*z*) and (*y*-*z*) are shown in Fig. 3 and Fig. 4, respectively. As shown in Fig. 4, the magnets are positioned symmetrically about $y = 0$ (if not, the problem can also be solved). The whole domain of the field problem is divided into three rectangular regions: the PMs region (region I), the air-gap region (region II) and the copper region (region III). In the proposed analysis, the edge effects are still taken into account thanks to the 3-D resolution in Cartesian coordinates (x, *y*, *z*).

A. Boundary Conditions

In order to solve this three-dimensional boundary value problem, we have to define boundary conditions in the *x* and *y*-directions. Interface conditions in the *z*-direction will then be used to calculate the unknown coefficients which appear in the general solutions for each region.

Due to alternate polarity of the PMs and since the eddy-currents reflect the poles structure of the exciting field, the magnetic problem presents an odd periodic boundary condition in the *x*-direction. The studied domain is then limited by $-\tau/2 \le x \le \tau/2$, as shown in Fig. 3, and for each region *i* the magnetic field boundary condition is given by

$$\mathbf{H}_i(-\tau/2, y, z) = -\mathbf{H}_i(\tau/2, y, z) \quad \text{with} \quad (i = I, II, III) \tag{2}$$

where $\mathbf{H}_i$ is the magnetic field strength in region *i*. As we consider the soft-magnetic yokes with infinite permeability (Fig. 3), the tangential components of the magnetic field strength are zero at $z = 0$ and $z = z_t$

$$\mathbf{H}_I \times \mathbf{e_z} = 0 \ \text{ at } \ z = 0 \tag{3}$$

$$\mathbf{H}_{III} \times \mathbf{e_z} = 0 \ \text{ at } \ z = z_t \ \text{ with } \ z_t = b + c + d \tag{4}$$

This limits the number of region where the magnetic field has to be determined (the magnetic field strength is null in the iron parts). This hypothesis can be regarded as accurate because the thicknesses *a* and *e* of the back-iron (see Fig. 1 and Fig. 2) must be determined to avoid magnetic saturation [6].

We also need to fix boundary conditions in the *y*-direction to solve this 3-D problem. As shown in Fig. 4, the studied domain is then truncated by artificial boundaries such as $-H/2 \le y \le H/2$. To solve the problem, we impose perfect magnetic boundary condition at $y = \pm H/2$. This leads to homogeneous Dirichlet boundary conditions for the *x* and *z* components of the magnetic field strength

$$\mathbf{H}_i \times \mathbf{e_y} = 0 \ \text{ at } \ y = \pm H/2 \ \text{ with } \ i = I, II, III \tag{5}$$

Of course, this artificial boundary condition will have an impact on the accuracy of the magnetic field determination and therefore on the torque prediction, compared to the original unbounded problem. However this impact will be limited if $H > L$, which corresponds to a well-designed eddy-current coupling [6], [7]. This will be discussed in section V.

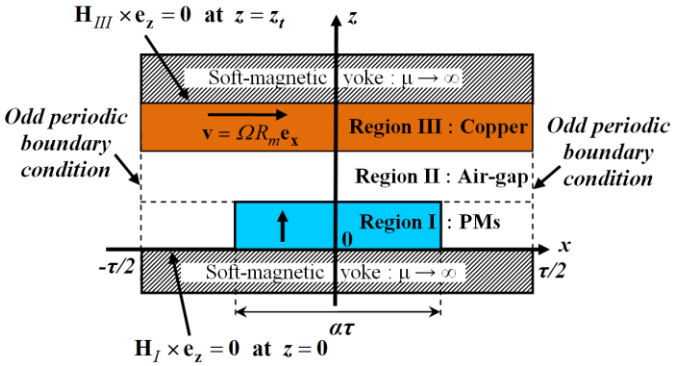

Fig. 3. Sectional view of the linear eddy-current coupling in the (*x*-*z*) plane for one pole pitch and its boundary conditions.

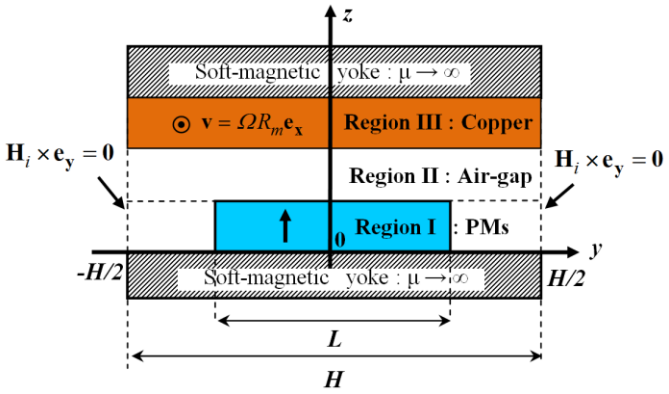

Fig. 4. Sectional view of the linear eddy-current coupling in the (*y*-*z*) plane and its boundary conditions at $y = \pm H/2$.

B. General Solution in the Non Conductive Regions (Region I and II)

The magnetic field in region I and II (PMs and air-gap) satisfies the basic equations of magnetostatic

$$\nabla \cdot \mathbf{B}_i = 0 \qquad \nabla \times \mathbf{H}_i = 0 \qquad (i = I \text{ or } II) \tag{6}$$

where $\mathbf{B}_i$ is the magnetic flux density in region *i*. From (6), the magnetic field strength can be written in terms of a magnetic scalar potential Φ_i, which is defined as

$$\mathbf{H}_i = -\nabla \Phi_i \qquad (i = I \text{ or } II) \tag{7}$$

Rare earth PMs (NdFeB or SmCo) present a linear second quadrant characteristic such as

$$\mathbf{B}_i = \mu_0 \mu_r \mathbf{H}_i + \mu_0 \mathbf{M}_i \qquad (\mathbf{M}_i = 0 \ \ for \ \ i = II) \tag{8}$$

where μ_0 is the permeability of air, μ_r is the relative recoil permeability ($\mu_r = 1$), and $\mathbf{M}_i$ is the residual magnetization vector. Equations (6), (7) and (8) are combined to give

$$\nabla^2 \Phi_i = \nabla \cdot \mathbf{M}_i \tag{9}$$

Since the PMs are axially magnetized, the residual magnetization has only one component dependent on x and y and can be written as

$$\mathbf{M}_i = M_z(x,y)\mathbf{e_z} \tag{10}$$

The magnetization is independent on the z-direction, the Poisson equation (9) is then reduced to Laplace's equation in both zones (i = I) and (i = II). Partial differentials equation (PDE) to solve in regions I and II is written as follows in Cartesian coordinates

$$\frac{\partial^2\Phi_i}{\partial x^2}+\frac{\partial^2\Phi_i}{\partial y^2}+\frac{\partial^2\Phi_i}{\partial z^2}=0 \quad \text{with} \quad i=I,II \tag{11}$$

From (2) and (5), the boundary conditions for the PMs and air-gap regions in terms of magnetic scalar potential are given by

$$\begin{aligned}\Phi_i(-\tau/2,y,z) &= -\Phi_i(\tau/2,y,z)\\ \Phi_i(x,-H/2,z) &= \Phi_i(x,H/2,z)=0\end{aligned} \tag{12}$$

General solution of (11), which satisfies the boundary conditions (12), is obtained by using the method of separation of variables. The general solution is the same for both region (i = I, II). These solutions can be written in complex form as

$$\Phi_I(x,y,z)=\Re\left\{\sum_{n=1}^{\infty}\sum_{k=1}^{\infty}\overline{\Phi}_I(z)\cos\left(n\frac{\pi}{H}y\right)e^{jk\frac{\pi}{\tau}x}\right\} \tag{13}$$

$$\Phi_{II}(x,y,z)=\Re\left\{\sum_{n=1}^{\infty}\sum_{k=1}^{\infty}\overline{\Phi}_{II}(z)\cos\left(n\frac{\pi}{H}y\right)e^{jk\frac{\pi}{\tau}x}\right\} \tag{14}$$

with

$$\begin{aligned}\overline{\Phi}_I(z) &= \overline{A}_{nk}e^{\alpha_{nk}z}+\overline{B}_{nk}e^{-\alpha_{nk}z}\\ \overline{\Phi}_{II}(z) &= \overline{C}_{nk}e^{\alpha_{nk}z}+\overline{D}_{nk}e^{-\alpha_{nk}z}\end{aligned} \tag{15}$$

and

$$\alpha_{nk}=\sqrt{\left(\frac{n\pi}{H}\right)^2+\left(\frac{k\pi}{\tau}\right)^2} \tag{16}$$

where n and k are odd integers, $\Re$ denotes the real part of a complex number and $j=\sqrt{-1}$. The complex coefficients $\overline{A}_{nk}$, $\overline{B}_{nk}$, $\overline{C}_{nk}$ and $\overline{D}_{nk}$ will be determined by using the interface conditions in the z-direction.

Fig. 5 shows the magnetization distribution $M_z(x,y)$ along the x and y-direction. The magnetization distribution may be expressed in the form of a double Fourier series expansion (eigenfunctions of the previous boundary value problem) as follows

$$M_z(x,y)=\Re\left\{\sum_{n=1}^{\infty}\sum_{k=1}^{\infty}M_{nk}\cos\left(n\frac{\pi}{H}y\right)e^{jk\frac{\pi}{\tau}x}\right\} \tag{17}$$

with

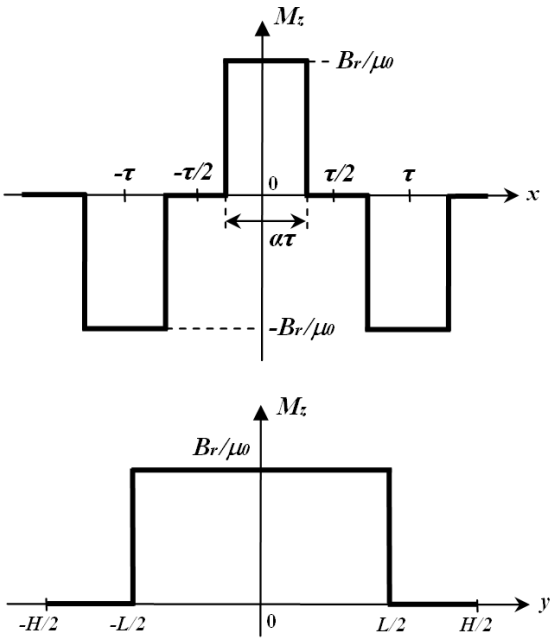

Fig. 5. Magnetization distribution along the x- and y-direction.

$$M_{nk}=\frac{4}{\tau H}\int_{-H/2}^{H/2}\int_{-\tau/2}^{\tau/2}M_z(x,y)\cos\left(k\frac{\pi}{\tau}x\right)\cos\left(n\frac{\pi}{H}y\right)dxdy \tag{18}$$

From (18) and using the magnetization distribution given in Fig. 5, we obtain

$$M_{nk}=\frac{16B_r}{\pi^2\mu_0 nk}\sin\left(k\alpha\frac{\pi}{2}\right)\sin\left(n\frac{\pi}{2}\frac{L}{H}\right) \tag{19}$$

where B_r is the remanent flux density.

C. General Solution in the Conductive Region (Region III)

The magnetic field in region III (copper) satisfies the quasi-static approximation of Maxwell equations

$$\begin{aligned}\nabla\times\mathbf{H}_{III}=\mathbf{J}_{III} \qquad \nabla\cdot\mathbf{B}_{III}=0\\ \nabla\times\mathbf{E}_{III}=-\frac{\partial\mathbf{B}_{III}}{\partial t}\end{aligned} \tag{20}$$

where $\mathbf{E}_{III}$ is the electric field strength and $\mathbf{J}_{III}$ the induced current density in region III. Ohm's law for moving conductor with reference to the stationary frame, which is fixed to the magnets disc, is expressed as

$$\mathbf{J}_{III}=\sigma\left(\mathbf{E}_{III}+\mathbf{v}\times\mathbf{B}_{III}\right) \tag{21}$$

where $\mathbf{v}$ is given by (1). Here, we consider only steady-state condition i.e. moving media with a constant speed. Moreover, the geometry of the moving part is invariant along the speed direction and the magnetic source is static (the reference frame is fixed to the PMs disc), so we can write [31]

$$\frac{\partial \mathbf{B}_{III}}{\partial t} = 0 \tag{22}$$

Therefore, the whole physical phenomena are time independent, and the eddy-current problem reduces to a magnetostatic problem. The problem in region III is solved by using a **H** - formulation (not any simplification is obtained by using a potential formulation for this 3D problem). From (20), (21) and (22), we obtain a second order differential equation

$$\nabla^2 \mathbf{H}_{III} = -\sigma\mu_0 \nabla \times \left(\mathbf{v} \times \mathbf{H}_{III} \right) \tag{23}$$

Written in Cartesian coordinates, (23) can be split into three partial differentials equations

$$\begin{aligned}
&\frac{\partial^2 H_{xIII}}{\partial x^2} + \frac{\partial^2 H_{xIII}}{\partial y^2} + \frac{\partial^2 H_{xIII}}{\partial z^2} = \sigma\mu_0 V_x \frac{\partial H_{xIII}}{\partial x} \\
&\frac{\partial^2 H_{yIII}}{\partial x^2} + \frac{\partial^2 H_{yIII}}{\partial y^2} + \frac{\partial^2 H_{yIII}}{\partial z^2} = \sigma\mu_0 V_x \frac{\partial H_{yIII}}{\partial x} \\
&\frac{\partial^2 H_{zIII}}{\partial x^2} + \frac{\partial^2 H_{zIII}}{\partial y^2} + \frac{\partial^2 H_{zIII}}{\partial z^2} = \sigma\mu_0 V_x \frac{\partial H_{zIII}}{\partial x}
\end{aligned} \tag{24}$$

where V_x is the velocity of the conducting plate along the *x*-direction. By using the method of separation of variables with the boundary conditions (2) and (5), the general solution for the *x* and *z* components of the magnetic field strength can be written as

$$\begin{aligned}
H_{xIII}(x,y,z) &= \Re\left\{ \sum_{n=1}^{\infty}\sum_{k=1}^{\infty} \overline{H}_{xIII}(z) \cos\left(n\frac{\pi}{H} y \right) e^{jk\frac{\pi}{\tau}x} \right\} \\
H_{zIII}(x,y,z) &= \Re\left\{ \sum_{n=1}^{\infty}\sum_{k=1}^{\infty} \overline{H}_{zIII}(z) \cos\left(n\frac{\pi}{H} y \right) e^{jk\frac{\pi}{\tau}x} \right\}
\end{aligned} \tag{25}$$

with

$$\begin{aligned}
\overline{H}_{xIII}(z) &= \overline{E}_{nk} e^{\gamma_{nk} z} + \overline{F}_{nk} e^{-\gamma_{nk} z} \\
\overline{H}_{zIII}(z) &= \overline{G}_{nk} e^{\gamma_{nk} z} + \overline{H}_{nk} e^{-\gamma_{nk} z}
\end{aligned} \tag{26}$$

and

$$\gamma_{nk} = \sqrt{\left(\frac{n\pi}{H} \right)^2 + \left(\frac{k\pi}{\tau} \right)^2 + j\sigma\mu_0 V_x \frac{k\pi}{\tau}} \tag{27}$$

Furthermore, we know that $\nabla \cdot \mathbf{H}_{III} = 0$, which gives the following relation to compute H_{yIII} from H_{xIII} and H_{zIII}

$$H_{yIII}(x,y,z) = -\int \left(\frac{\partial H_{xIII}}{\partial x} + \frac{\partial H_{zIII}}{\partial z} \right) dy \tag{28}$$

By using (25), (26) and (28), we obtain

$$H_{yIII}(x,y,z) = \Re\left\{ \sum_{n=1}^{\infty}\sum_{k=1}^{\infty} \overline{H}_{yIII}(z) \sin\left(n\frac{\pi}{H} y \right) e^{jk\frac{\pi}{\tau}x} \right\} \tag{29}$$

with

$$\overline{H}_{yIII}(z) = -\frac{H}{n\pi}\left(j\frac{k\pi}{\tau}\overline{H}_{xIII}(z) + \frac{d\overline{H}_{zIII}(z)}{dz} \right) \tag{30}$$

The unknown coefficients $\overline{E}_{nk}$ to $\overline{H}_{nk}$ in (26) will be solved by using the field continuity between regions II and III and the boundary condition (4).

D. Interface Conditions

As shown in (15) and (26), we have eight unknown coefficients to determine. This means that we need eight independent linear equations. Three equations are obtained by considering (3) and (4)

$$\begin{aligned}
&\Phi_I(x,y,0) = 0 \\
&H_{xIII}(x,y,z_t) = 0 \\
&\frac{\partial H_{zIII}(x,y,z_t)}{\partial z} = 0
\end{aligned} \tag{31}$$

The normal component of the magnetic flux density and the tangential component of the magnetic field strength are continuous between region I and II (at $z = b$) and between regions II and III ($z = b + c$). Knowing that all regions have the same magnetic permeability ($\mu_r = 1$), we obtain five independent linear equations including one with the source term $M_z(x,y)$

$$\begin{aligned}
&\Phi_I(x,y,b) = \Phi_{II}(x,y,b) \\
&\frac{\partial \Phi_I(x,y,b)}{\partial z} = \frac{\partial \Phi_{II}(x,y,b)}{\partial z} - M_z(x,y) \\
&\frac{\partial \Phi_{II}(x,y,b+c)}{\partial x} = -H_{xIII}(x,y,b+c) \\
&\frac{\partial \Phi_{II}(x,y,b+c)}{\partial y} = -H_{yIII}(x,y,b+c) \\
&\frac{\partial \Phi_{II}(x,y,b+c)}{\partial z} = -H_{zIII}(x,y,b+c)
\end{aligned} \tag{32}$$

By using the eight independent linear equations given above, all the unknown constants can be obtained. Developments are given in the appendix. After a lot of calculations, (15), (26) and (30) can be rewritten as follows where the unknown coefficients have been replaced by their expressions

$$\begin{aligned}
\overline{\Phi}_I(z) &= \frac{M_{nk}}{\alpha_{nk}} \bar{r} \sinh\left(\alpha_{nk} z \right) \\
\overline{\Phi}_{II}(z) &= \frac{M_{nk}}{\alpha_{nk}} \left\{ \sinh\left(\alpha_{nk} \left(z - b \right) \right) + \bar{r} \sinh\left(\alpha_{nk} z \right) \right\}
\end{aligned} \tag{33}$$

and

$$\begin{aligned}\overline{H}_{xIII}(z) &= -j\frac{k\pi}{\tau}\frac{M_{nk}}{\alpha_{nk}}\bar{q}\sinh\left(\gamma_{nk}\left(z-z_t\right)\right)\\ \overline{H}_{yIII}(z) &= \frac{n\pi}{H}\frac{M_{nk}}{\alpha_{nk}}\bar{q}\sinh\left(\gamma_{nk}\left(z-z_t\right)\right)\\ \overline{H}_{zIII}(z) &= -\alpha_{nk}\frac{M_{nk}}{\gamma_{nk}}\bar{q}\cosh\left(\gamma_{nk}\left(z-z_t\right)\right)\end{aligned} \tag{34}$$

where M_{nk} is given by (19), $\bar{r}$ and $\bar{q}$ are given in the appendix (A.3). The magnetic field in all regions is now fully defined. It is therefore possible to compute the induced currents in the moving conducting plate.

E. Eddy-Currents Expressions

The induced currents in the conducting plate are obtained from the Ampere Law

$$\mathbf{J}_{III} = \nabla\times\mathbf{H}_{III} \tag{35}$$

By substituting (25), (29), (34) in (35), we obtain the three components of the induced current density

$$\begin{aligned}J_{xIII}(x,y,z) &= \Re\left\{\sum_{n=1}^{\infty}\sum_{k=1}^{\infty}\overline{J}_{xIII}(z)\sin\left(n\frac{\pi}{H}y\right)e^{jk\frac{\pi}{\tau}x}\right\}\\ J_{yIII}(x,y,z) &= \Re\left\{\sum_{n=1}^{\infty}\sum_{k=1}^{\infty}\overline{J}_{yIII}(z)\cos\left(n\frac{\pi}{H}y\right)e^{jk\frac{\pi}{\tau}x}\right\}\\ J_{zIII}(x,y,z) &= 0\end{aligned} \tag{36}$$

with

$$\begin{aligned}\overline{J}_{xIII}(z) &= \frac{n\pi}{H}M_{nk}\bar{q}\left(\frac{\gamma_{nk}}{\alpha_{nk}}-\frac{\alpha_{nk}}{\gamma_{nk}}\right)\cosh\left(\gamma_{nk}\left(z-z_t\right)\right)\\ \overline{J}_{yIII}(z) &= j\frac{k\pi}{\tau}M_{nk}\bar{q}\left(\frac{\gamma_{nk}}{\alpha_{nk}}-\frac{\alpha_{nk}}{\gamma_{nk}}\right)\cosh\left(\gamma_{nk}\left(z-z_t\right)\right)\end{aligned} \tag{37}$$

With the adopted assumptions, we can note that the induced currents flow only in *x*-*y* planes (laminar eddy currents). As expected, we can observe that the *y*-component of the induced current is null at $y = \pm H/2$.

IV. Torque and Axial-Force Expressions

A. Electromagnetic Torque

The electromagnetic torque is obtained using the Maxwell stress tensor. A rectangular surface of dimensions 2τ and H, placed at $z = b$ in the air-gap region is taken as the integration surface ($z = b$ gives the simplest expression for the magnetic field in the air-gap, i.e. (33)). The electromagnetic torque T_e can then be expressed as follows

$$T_e = pR_m\mu_0\int_{-\tau}^{\tau}\int_{-H/2}^{H/2}H_{xII}(x,y,b)H_{zII}(x,y,b)\,dxdy \tag{38}$$

where H_{xII} and H_{zII} can be derived from (14) and (33), knowing that $\mathbf{H}_{II} = -\nabla\Phi_{II}$. From (38), we obtain a closed-form expression for the torque which depends directly on the physical and geometrical parameters

$$T_e = \frac{1}{2}\mu_0 p^2\tau H\Re\left\{\sum_{n=1}^{\infty}\sum_{k=1}^{\infty}jk\frac{M_{nk}^2}{\alpha_{nk}}\bar{r}\sinh\left(\alpha_{nk}b\right)\right\} \tag{39}$$

where n and k are odd integers, and $\bar{r}$ is given in the appendix.

B. Axial-Force

Axial magnetic force is an important parameter for the design of an axial magnetic coupling. This force must be known because it affects directly the rotor structure and bearings. For eddy-current couplings, the axial force can be attractive or repulsive and depends of the slip speed [14]. By using the Maxwell stress tensor with the same integration surface as previously used for the torque calculation, the axial force expression is given by

$$F_z = p\mu_0\int_{-\tau}^{\tau}\int_{-H/2}^{H/2}\frac{H_{zII}^2(x,y,b)-H_{xII}^2(x,y,b)-H_{yII}^2(x,y,b)}{2}dxdy \tag{40}$$

By substituting H_{xII}, H_{yII}, and H_{zII} in (40), we obtain a closed-form expression for the axial force

$$F_z = \frac{1}{4}\mu_0 p\tau H\sum_{n=1}^{\infty}\sum_{k=1}^{\infty}M_{nk}^2\left(1+r^2+\left(\bar{r}+\bar{r}^*\right)\cosh\left(\alpha_{nk}b\right)\right) \tag{41}$$

where $\bar{r}^*$ is the complex conjugate of $\bar{r}$ which is given in the appendix.

V. Comparison with 3-D Finite Element Simulations

In order to show the effectiveness of the proposed 3-D analytical model, the results are compared with those obtained from 3-D finite-element model (FEM). The finite-element simulations (COMSOL Multiphysics® with **A**-φ formulation) are conducted by considering the reaction field due to the motional induced currents and the actual geometry of the coupling (i.e. cylindrical structure as shown in Fig. 1). The mesh in the different regions has been refined until convergent results are obtained. The air surrounding the magnetic coupling is considered in the FEM simulation (infinite box surround the system). As the soft-magnetic yoke thickness (*a* and *e* in Fig. 1) are designed to avoid magnetic saturation, we consider a relative permeability μ_r = 1000 for the ferromagnetic parts. This value is a good approximation for AISI-1010 (low carbon steel) that has been used for the

experimental validation. Low carbon steel such as AISI-1010 presents a high permeability in the linear region (relative permeability greater than 1000 for $B < 1.5$T) and a high level of saturation ($B_s \simeq 1.8$T).

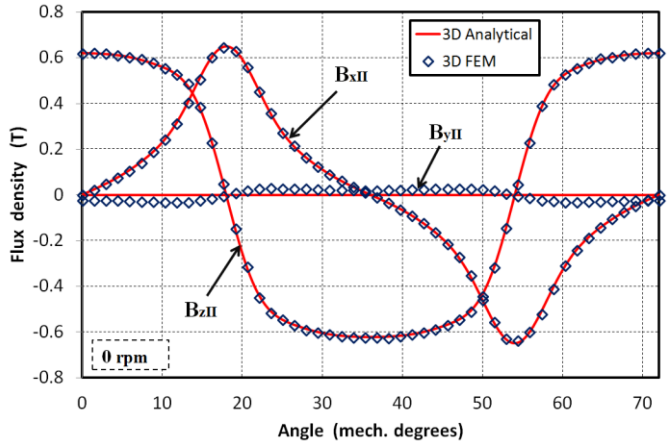

(a)

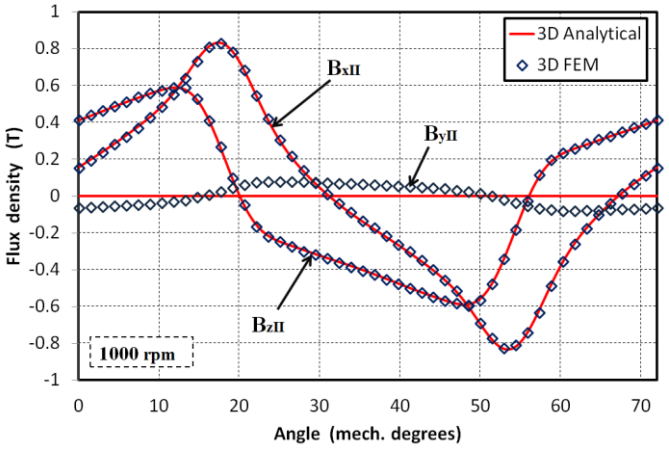

(b)

Fig. 6. Flux density distribution along the x-direction in the middle of the airgap ($z = b+c/2$) at $y = 0$ for c = 3 mm. (a) 0 rpm. (b) 1000 rpm.

TABLE I
PARAMETERS OF THE STUDIED EDDY-CURRENT COUPLING

Symbol	Quantity	value
R_1	Inner radius of the magnets	30 mm
R_2	Outer radius of the magnets	60 mm
R_0	Inner radius of the conducting plate	15 mm
R_3	Outer radius of the conducting plate	75 mm
a	Thickness of the back-iron (magnets side)	10 mm
b	Magnets thickness	10 mm
c	Air-gap length	variable
d	Conducting plate thickness	5 mm
e	Thickness of the back-iron (copper side)	8 mm
α	PMs pole-arc to pole-pitch ratio	0.9
p	Pole-pairs number	5
B_r	Remanence of the permanent magnets (NdFeB)	1.25 T
σ	Conductivity of the conducting plate (copper)	57 MS/m
N	Number of harmonic terms in the x-direction	10
K	Number of harmonic terms in the y-direction	10

The geometrical parameters of the studied magnetic coupling are given in Table I. With these parameters and considering $c = 3$ mm, we obtain a torque of about 10 Nm for a slip speed of 150 rpm [6]. The radial length of the copper is chosen to be $H = 60$ mm, which corresponds to 30 mm additional length compare to the active length of the magnets (15 mm on each side) i.e. $H = 2L$. It has been shown in [6], [7] that the performances of eddy-current couplings are greatly improved if $H \simeq L + \tau$, which gives $H \simeq 2L$ for the studied coupling. The analytical results given in the next developments have been computed with a finite number of harmonic terms N and K as indicated in Table I.

A. Flux Density Distribution in the Air-Gap

Fig. 6 shows the flux density distribution along the x-direction (circumferential direction) at $z = b + c/2$ (middle of the air-gap), $y = 0$ (mean radius) for two values of the angular speed: 0 rpm and 1000 rpm. The air-gap is fixed at $c = 3$ mm. Good agreements can be observed between the 3-D analytical results and the 3-D FEM simulations. It can be seen that B_{yII} presents a slight variation around zero with the 3-D FEM simulations, whereas it is null with the analytical model. This difference is due to the curvature effects which are not taken into account in the analytical modeling. Fig. 6(b) clearly shows that the reaction field due to the induced currents in the copper disc tends to distort the flux density for 1000 rpm.

Fig. 7 shows the flux density distribution along the y-direction (radial direction) at $z = b + c/2$ and $x = 0$. Once again, the agreement between analytical and numerical results is good. We can observe that B_{xII} is no longer equal to zero as the slip speed increases. This result is well predicted by the analytical model. As expected, a reduction in the magnitude of B_{zII} occurs as a result of the reaction field. Furthermore, Fig. 7(b) shows that the analytical value of B_{yII} is slightly different over the edges of the copper ($r = 15$ mm and $r = 75$ mm) compared to 3-D FEM. This is due to the artificial boundary condition (5) used to solve this 3-D problem. Indeed, (5) imposes that $B_{xIII} = B_{zIII} = 0$ at $y = \pm H/2$ but $B_{yIII} \neq 0$ (only $dB_{yIII}/dy = 0$ is imposed at $y = \pm H/2$ with the proposed analytical model because $\nabla \cdot \mathbf{B}_{III} = 0$). This is the main drawback of the analytical model compared to the real geometry (unbounded in the radial direction).

B. Current Density Distribution

Fig. 8 shows the eddy-current distribution (showed as arrows) in the middle of the copper ($z = b + c + d/2$) obtained with 3-D FEM for a slip speed of 1000 rpm. It can be seen that the induced currents flow along closed paths (loops) inside the copper disc. From Fig. 8, one can observe that the induced currents in the circumferential direction (these currents do not contribute to the torque) are mainly situated outside the useful area corresponding to the magnet's active length ($L = R_2 - R_1$). We will show in the next subsection that this additional copper length has a significant effect on the torque value.

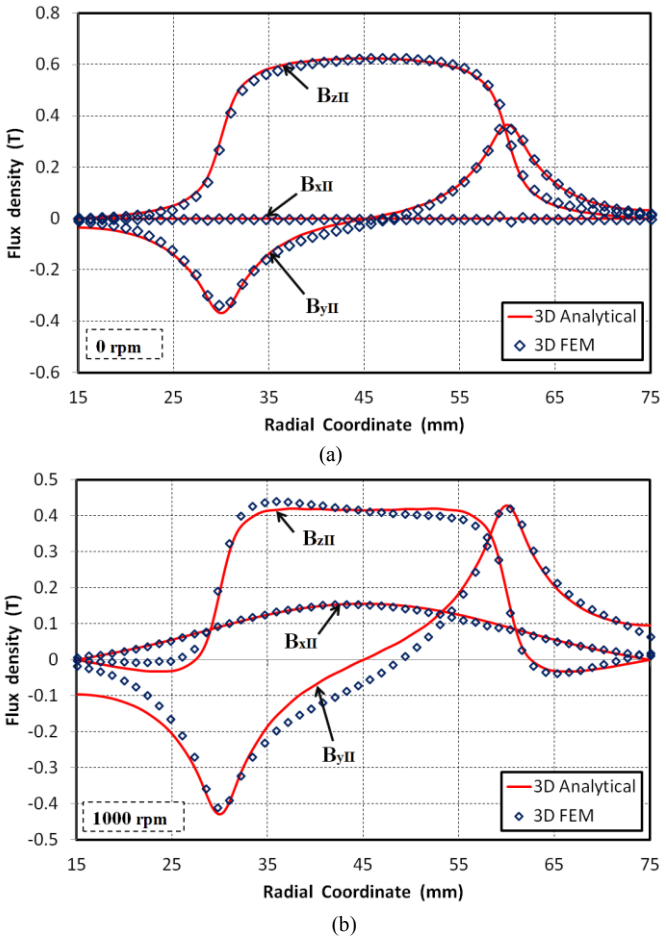

Fig. 7. Flux density distribution along the *y*-direction in the air-gap ($z = b+c/2$) at $x = 0$ for c = 3 mm. (a) 0 rpm. (b) 1000 rpm.

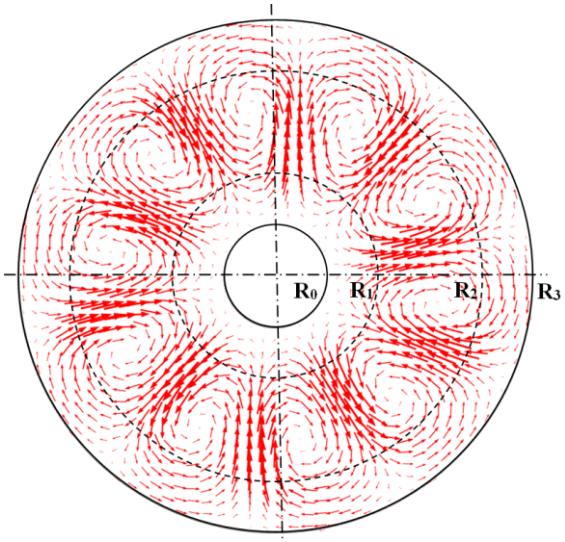

Fig. 8. Eddy-current density distribution in the middle of the copper at 1000 rpm obtained by 3-D FEM (showed as arrows).

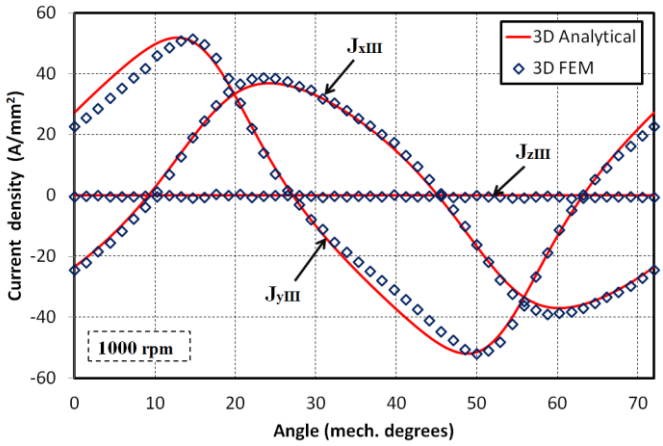

Fig. 9. Eddy-current density distribution along the *x*-direction in the middle of the copper $z = b+c+d/2$ at $y = L/2$ ($r = R_2$) for $c = 3$ mm (1000 rpm).

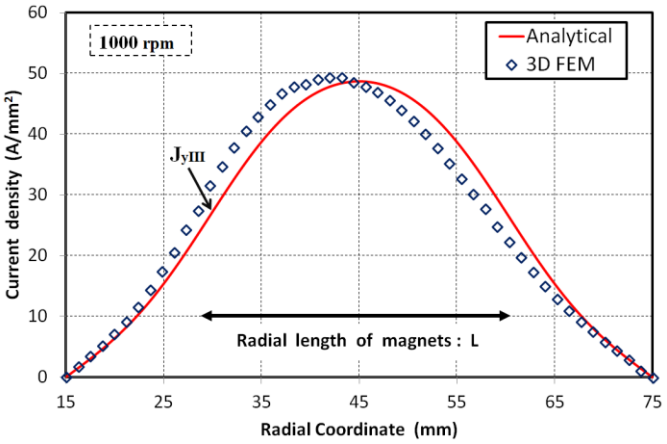

Fig. 10. Eddy-current density distribution (J_{yIII}) along the *y*-direction in the middle of the copper $z = b+c+d/2$ at $x = 0$ ($\theta = 0$) for $c = 3$ mm (1000 rpm).

Fig. 9 compares the eddy-current density distribution along the *x*-direction at $y = L/2$ (outer edge of the magnet, i.e. $r = R_2$ as shown in Fig. 8) obtained with 3-D FEM and with the proposed analytical formulas (36) and (37), for a slip speed of 1000 rpm. The results obtained with the 3-D FEM confirm that the *z* component of the current density (J_{zIII}) is null, as provided by the analytical model (36). As shown in Fig. 9, J_{xIII} and J_{yIII} are well predicted by the 3-D analytical model in terms of amplitudes and waveforms. Fig. 10 shows the eddy-current distribution (*y* component) along the *y*-direction (radial direction) at $x = 0$ ($\theta = 0$, see Fig. 8). Fig. 10 clearly shows the ability of the proposed model to predict the induced currents distribution in the *y*-direction. The small difference between the analytical result and the 3D FEM simulation is due to the curvature effects.

Based on these preliminary results and knowing that the 3-D FEM simulations take into account the actual geometry of the coupling, it can be stated that the assumption of linearization at the mean radius used in the 3-D analytical model can be considered as valid for the studied coupling. It is worth noting that the curvature effects will be low if $L/\tau \simeq 1$ (for the studied coupling, we have $L/\tau = 1.06$ for $p = 5$). Discussions about it will be developed in subsection D.

C. Torque and Axial Force

The torque versus slip speed for the studied coupling (Table I) is given in Fig. 11. Three values of the air-gap have been considered (c = 3 mm, c = 5 mm, and c = 7 mm). As expected, the peak torque decreases when the air-gap increases. For the studied coupling, the peak torque corresponds to a slip speed of around 1000 rpm for all the air-gap values. It is worth noting that the computation time needed to compute the torque-speed characteristic given in Fig. 11 is more than 3 hours with the 3-D FEM (30 points) whereas this characteristic is immediately obtained (below 50 ms) by using the analytical formula (39), with the first 10 odd harmonic terms in the x and y-direction.

Fig. 12 shows the axial force acting on one side of the coupling. For low speed values (below 600 rpm), the attractive force between magnets and the opposite soft-magnetic yoke is dominant. Then, as the speed increases, the induced currents in the copper disc produce a repulsive force that becomes dominant for large speed values [14]. As shown in Fig. 11 and Fig. 12, the torque and the axial force are well predicted by the proposed analytical formulas.

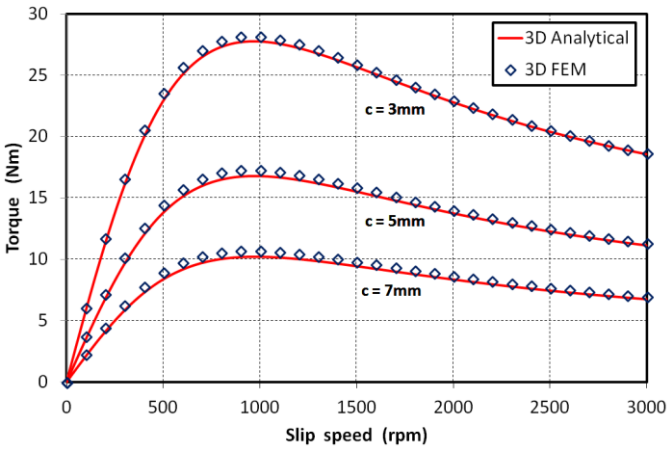

Fig. 11. Torque versus slip speed for three values of the air-gap length (c = 3mm, c = 5mm, and c = 7mm).

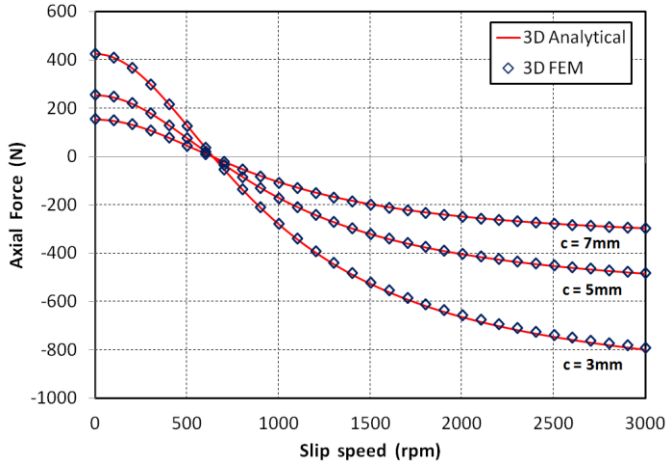

Fig. 12. Axial force versus slip speed for three values of the air-gap length (c = 3 mm, c = 5 mm, and c = 7 mm).

D. Influence of Geometrical Parameters

In order to show the limits of the proposed torque formula (39), we have varied some important geometrical parameters (pole-pairs number, ratio of the radial copper length to the radial magnet length i.e. H/L). The other geometrical parameters are those given in Table I. Here we consider an air-gap of 3 mm and a slip speed of 300 rpm.

Torque versus the pole-pairs number (with H/L = 2) is given in Fig. 13. Errors between analytical and numerical results are never greater than 15% and occur for large value of the pole-pairs number. This is mainly due to the curvature effects which are more significant when the number of pole-pairs increases (the other parameters are the ones given in Table I). For a given air gap, the error introduced by the linearization assumption depends on the radial excursion of the magnets L and on the pole pitch at the mean radius τ [28]. If $L/\tau \simeq 1$, the curvature effects are not significant and the mean radius hypothesis can be considered as correct. For the studied problem, $L/\tau \simeq 1$ corresponds to p = 4-5 and we can observe in Fig. 13 that the torque is well predicted under this condition. For p = 10, we obtain L/τ = 2.12 (curvature effects are much significant in this case) which leads to an error of around 15% (Fig. 13). It can be seen in Fig. 13 that an optimum value exists for the pole-pairs number (p = 4). This optimum value is well predicted by using the torque formula (39).

Fig. 14 shows the torque versus the ratio H/L. The torque increases rapidly at first and then becomes almost constant for $H/L \geq 2$. An improvement of about 50% is obtained on the torque value in adopting H/L = 2 instead of H/L = 1. Furthermore, one can note a significant error (greater than 30%) on the torque prediction when H/L = 1. This is due to the artificial boundary condition (5) used in the analytical model compared to the unbounded problem solved with 3-D FEM. This is the main drawback of the proposed 3D analytical model. The torque formula (39) should be handled with care when H/L $\simeq$ 1. However, the influence of this artificial boundary condition on the torque prediction will be limited if $H > L$, that corresponds to a well-designed eddy-current coupling where $H \simeq L + \tau$ [7].

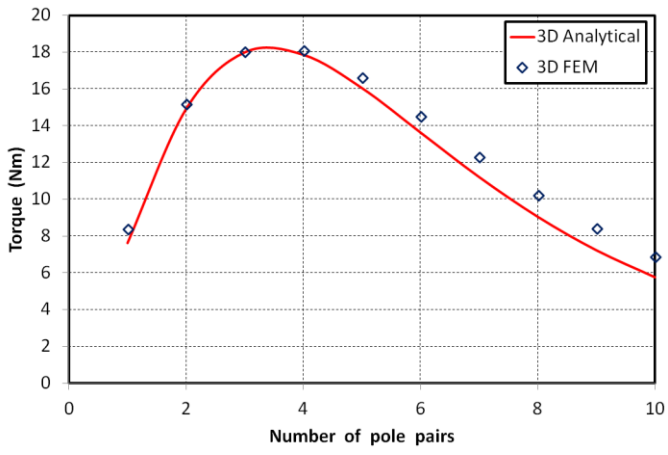

Fig. 13 Torque versus number of pole pairs at 300 rpm for c = 3 mm.

VI. Comparison with Measurement

For the experimental validation, we have manufactured a prototype as shown in Fig. 15. The eddy-current coupling is made with 10 sector type NdFeB magnets (grade N40) glued on the soft-magnetic yoke, the other face is made with a copper plate screwed on the back-iron (AISI-1010 carbon steel), as respectively shown in Fig. 15(a) and Fig. 15(b). Fig. 15(c) shows the prototype placed on the test bench. The geometrical parameters are those given in Table I.

The magnetic coupling is placed between two electrical motors (DC motors of 3kW, 3000 rpm). For the experimental tests, one shaft is locked (copper side), and the other shaft can rotate (magnets side). The eddy-current coupling then acts as a brake for the DC machine. The speed is measured with an encoder, and is controlled by changing the voltage applied to the armature of the DC motor. The torque is obtained from the armature current measurement (the torque constant of the DC motor is 1,35Nm/A).

For the experimental verification, the air-gap is fixed to c = 7 mm. With this air-gap value, Fig. 11 shows that the maximal torque is around 10 Nm that corresponds to the nominal torque value of the DC machine in used.

A. Air-gap Flux Density Measurement

The air-gap flux density is measured by a Gaussmeter based on Hall effect. The output of the Gaussmeter has a BNC-connector which can be linked to a data acquisition system.

The flux density along the *x*-direction (circumferential direction) has been measured for 0 rpm and 800 rpm. The Hall probe has been placed in the middle of the air-gap and at the mean radius. The results are given in Fig. 16 and Fig. 17 (only B_{xII} has been measured for 800 rpm). Very good agreements are found between experimental results and the analytical predictions. The distortion and phase shift for the air-gap flux density B_{zII} is clearly shown by comparing Fig. 16 and Fig. 17. These are due to the induced current reaction field at 800 rpm.

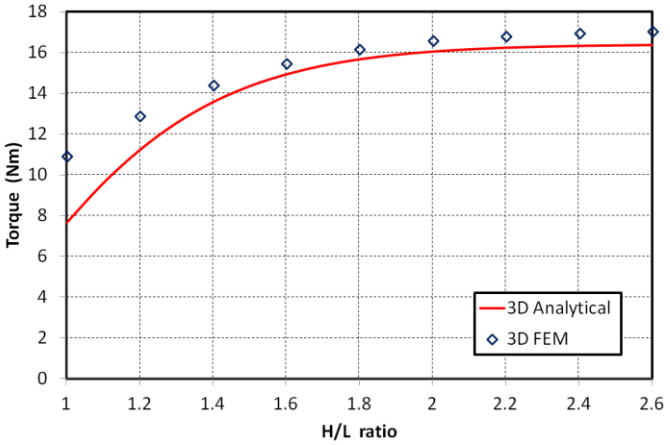

Fig. 14 Torque versus the ratio *H*/*L* at 300 rpm for *c* = 3 mm.

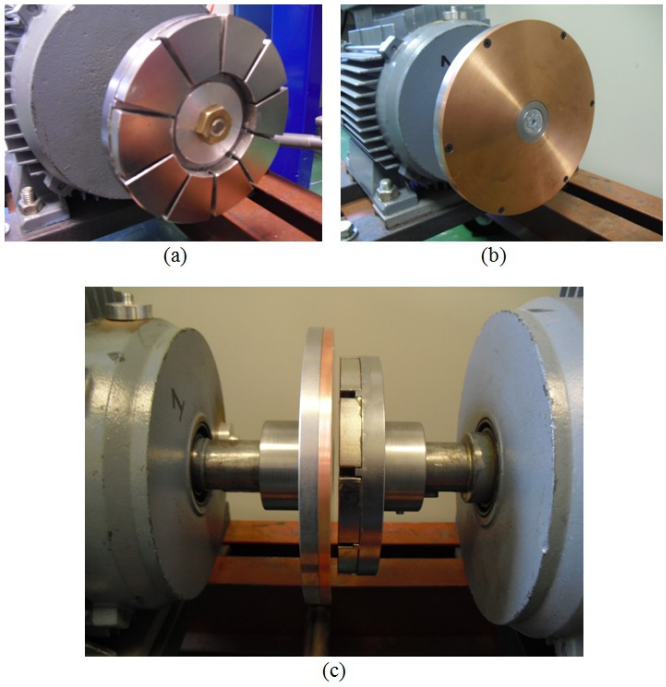

Fig. 15. Eddy-current coupling prototype: (a) PMs side with *p* = 5, (b) copper side, (c) magnetic coupling placed on the test bench

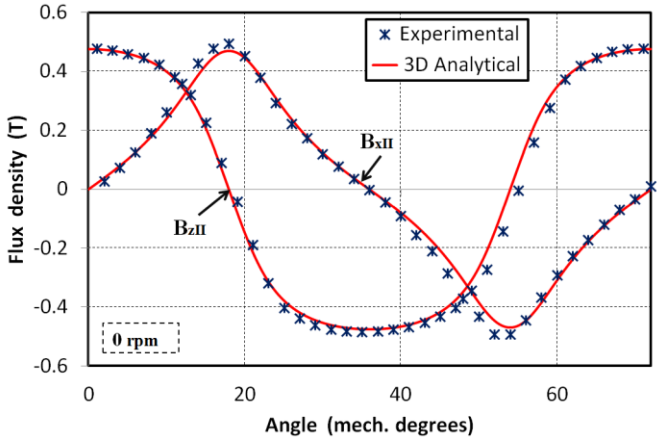

Fig. 16. Measured and computed magnetic flux density along the *x*-direction (middle of the air-gap, at the mean radius) at 0 rpm for *c* = 7 mm.

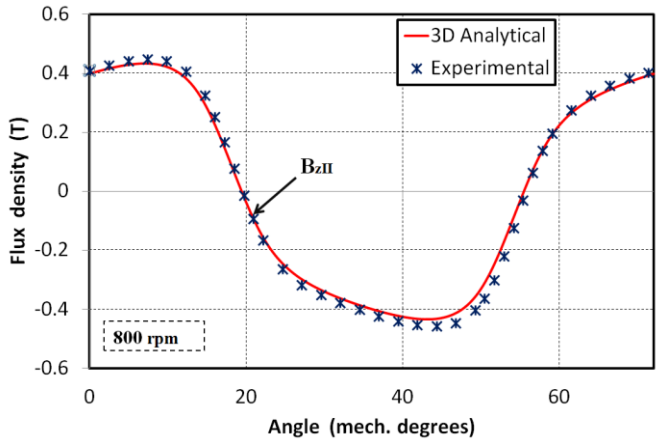

Fig. 17. Measured and computed axial flux density along the *x*-direction (middle of the air-gap, at the mean radius) at 800 rpm for *c* = 7 mm.

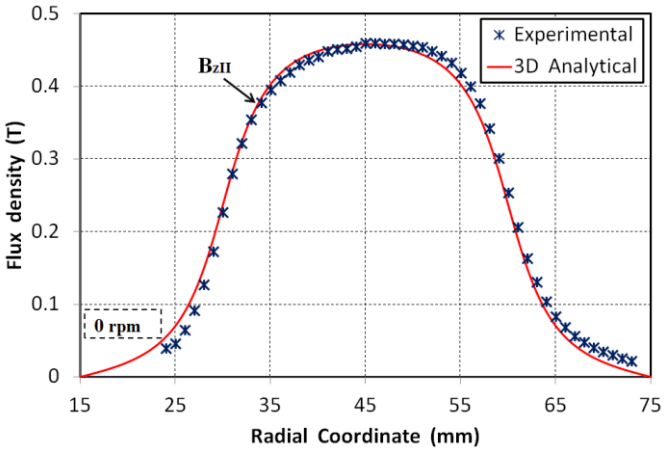

Fig. 18. Measured and computed flux density along a radial line in the middle of the air-gap at a center line of a pole for c = 7 mm.

We have also measured the radial dependence of the axial flux density at a center line of a pole (for 0 rpm). The results are shown in Fig. 18. We can observe that the axial flux density shows large variations along the radial expanse of the copper disc. The slight discrepancy between the 3D analytical model and experimental tests is due to the curvature effects which are not taken into account in the analytical model (the flux density is no longer symmetrical about r = 45 mm with 3-D FEM). The little jump in the flux density that can be observed in Fig. 18 (around r = 45 mm) is probably due to a measurement error.

B. Torque versus Slip Speed

Fig. 19 shows a comparison between the analytically predicted torque-slip characteristic and the measured data. For the analytical determination, we have considered a constant copper conductivity σ = 57MS/m, which corresponds to a working temperature of around 35°C. During the tests, the surface temperature of the copper was measured by using a K-type thermocouple and the temperature was limited to 35°C. For large slip speed values, the torque measurement must be done very quickly because the copper temperature increases rapidly, which affects the torque value.

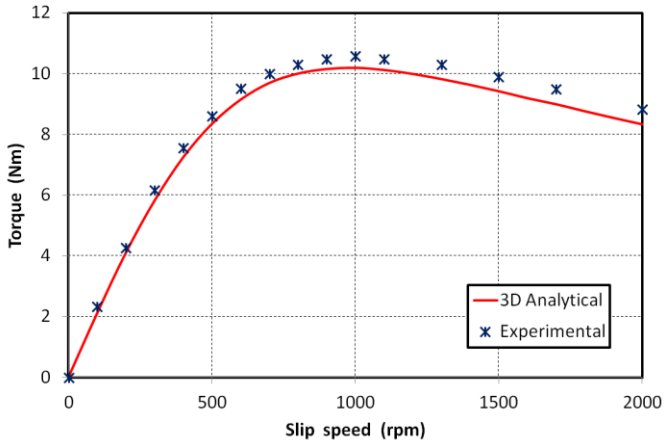

Fig. 19. Torque versus slip speed for c = 7 mm.

Fig. 19 shows that the experimental data are very close to the analytical predictions. Deviations are not greater than 5% throughout the slip speed, which confirms the validity of the proposed model with its assumptions.

VII. Conclusion

In this paper, a 3-D analytical model has been developed to predict flux density distribution, induced currents, torque and axial force for axial-flux permanent magnets eddy current couplings and brakes under steady state condition. To solve this three dimensional boundary value problem, a magnetic scalar potential formulation has been used in the non conductive regions (magnets, air-gap), and a magnetic field strength formulation has been adopted in the conductive region (copper). The torque and the axial force formulas have been obtained from the Maxwell stress tensor method.

Comparisons with 3-D FEM simulations on the one hand and experimental tests on the other hand have shown the ability of the torque formula in the determination of the coupling performances if $H > L$. It is shown that the proposed model is very accurate (the error is less than 5% for the torque-speed characteristic whatever the slip value) and very fast in terms of computation time. The determination of the torque-speed characteristic is obtained in few tens of millisecond whereas it takes several hours with 3-D FEM. The proposed model offers a new powerful tool in the design and optimization process of eddy-current couplings or brakes.

Appendix

From (31), we obtain three equations for the unknown coefficients

$$\begin{aligned}\overline{B}_{nk} &= -\overline{A}_{nk}\\ \overline{F}_{nk} &= -\overline{E}_{nk}e^{2\gamma_{nk}z_t}\\ \overline{H}_{nk} &= \overline{G}_{nk}e^{2\gamma_{nk}z_t}\end{aligned} \tag{A.1}$$

From (32), we obtain five equations for the unknown coefficients

$$\begin{aligned}&\overline{A}_{nk}e^{\alpha_{nk}b} + \overline{B}_{nk}e^{-\alpha_{nk}b} = \overline{C}_{nk}e^{\alpha_{nk}b} + \overline{D}_{nk}e^{-\alpha_{nk}b}\\ &\overline{A}_{nk}e^{\alpha_{nk}b} - \overline{B}_{nk}e^{-\alpha_{nk}b} = \overline{C}_{nk}e^{\alpha_{nk}b} - \overline{D}_{nk}e^{-\alpha_{nk}b} - \frac{M_{nk}}{\alpha_{nk}}\\ &-\frac{jk\pi}{\tau}\left(\overline{C}_{nk}e^{\alpha_{nk}(b+c)} + \overline{D}_{nk}e^{-\alpha_{nk}(b+c)}\right) = \overline{E}_{nk}e^{\gamma_{nk}(b+c)} + \overline{F}_{nk}e^{-\gamma_{nk}(b+c)}\\ &\frac{n\pi}{H}\left(\overline{C}_{nk}e^{\alpha_{nk}(b+c)} + \overline{D}_{nk}e^{-\alpha_{nk}(b+c)}\right) =\\ &\frac{H}{n\pi}\left\{\left(j\frac{k\pi}{\tau}\overline{E}_{nk} + \gamma_{nk}\overline{G}_{nk}\right)e^{\gamma_{nk}(b+c)} + \left(j\frac{k\pi}{\tau}\overline{F}_{nk} - \gamma_{nk}\overline{H}_{nk}\right)e^{-\gamma_{nk}(b+c)}\right\}\\ &-\alpha_{nk}\left(\overline{C}_{nk}e^{\alpha_{nk}(b+c)} - \overline{D}_{nk}e^{-\alpha_{nk}(b+c)}\right) = \overline{G}_{nk}e^{\gamma_{nk}(b+c)} + \overline{H}_{nk}e^{-\gamma_{nk}(b+c)}\end{aligned} \tag{A.2}$$

Expressions of $\bar{r}$ and $\bar{q}$ which appear in (33), (34), (37), (39) and (41) are given by

$$\bar{r} = -\frac{\cosh(\alpha_{nk}c)\sinh(\gamma_{nk}d) + \chi_{nk}\sinh(\alpha_{nk}c)\cosh(\gamma_{nk}d)}{\cosh(\alpha_{nk}(b+c))\sinh(\gamma_{nk}d) + \chi_{nk}\sinh(\alpha_{nk}(b+c))\cosh(\gamma_{nk}d)}$$

$$\bar{q} = \frac{\sinh(\alpha_{nk}b)}{\cosh(\alpha_{nk}(b+c))\sinh(\gamma_{nk}d) + \chi_{nk}\sinh(\alpha_{nk}(b+c))\cosh(\gamma_{nk}d)} \quad \text{(A.3)}$$

with

$$\chi_{nk} = \frac{\alpha_{nk}}{\gamma_{nk}} \quad \text{(A.4)}$$

where α_{nk} and γ_{nk} are given by (16) and (27), respectively.

REFERENCES

[1] E. J. Davies, "An experimental and theoretical study of eddy-current couplings and brakes," *IEEE Trans. Power App. Syst.*, vol. 82, no. 67, pp. 401-419, Aug. 1963.

[2] J. D. Edwards, B. V. Jayawant, W. R. C. Dawson, and D. T. Wright, "Permanent-magnet linear eddy-current brake with a nonmagnetic reaction plate," *Proc. IEE*, vol. 146, no. 6, pp. 627–631, Nov. 1999.

[3] A. Canova, and B. Vusini, "Design of axial eddy-current couplers," *IEEE Trans. Ind. Appl.*, vol. 39, no. 3, pp. 1725–1733, May/June 2003.

[4] S. Sharif, J. Faiz, and K. Sharif, "Performance analysis of a cylindrical eddy current brake," *IET Electr. Power Appl.,* vol. 6, no. 9, pp. 661-668, Nov. 2012.

[5] R. Yazdanpanah, and M. Mirsalim, "Axial-flux wound-excitation eddy-current brakes: analytical study and parametric modeling," *IEEE Trans. Magn.*, vol. 50, no. 6, p. 8000710, Jun. 2014.

[6] T. Lubin, and A. Rezzoug, "Steady-state and transient performance of axial-field eddy-current coupling," *IEEE Trans. Ind. Electron.*, vol. 62, no. 4, pp. 2287–2296, Apr. 2015.

[7] Z. Mouton, and M. J. Kamper, "Modeling and Optimal Design of an Eddy Current Coupling for Slip-Synchronous Permanent Magnet Wind Generators," *IEEE Trans. Ind. Electron.*, vol. 61, no. 7, pp. 3367–3376, Jul. 2014.

[8] T. W. Nehl, B. Lequesne, V. Gangla, S. A. Gutkowski, M. J. Robinson, and T. Sebastian, "Nonlinear two-dimensional finite element modeling of permanent magnet eddy current couplings and brakes," *IEEE Trans. Magn.,* vol.30, no.5, pp. 3000-3003, Sep. 1994.

[9] D. Albertz, S. Dappen, and G. Henneberger, "Calculation of the 3D non-linear eddy current field in moving conductors and its application to braking systems," *IEEE Trans. Magn.*, vol. 32, no. 3, pp. 768–771, May 1996.

[10] S. Jang, S. Lee, and S. Jeong, "Characteristic analysis of eddy-current brake system using the linear Halbach array," *IEEE Trans. Magn.*, vol. 38, no. 5, pp.2994-2296, Sep. 2002.

[11] S. E. Gay and M. Ehsani, "Parametric analysis of eddy-current brake performance by 3-D finite-element analysis," *IEEE Trans. Magn*., vol.42, no. 2, pp. 319–328, Feb. 2006.

[12] J. Bird, and T. A. Lipo, "Modeling the 3-D rotational and translational motion of a Halbach rotor above a split-sheet guideway," *IEEE Trans. Magn.*, vol. 45, no. 9, pp. 3233–3242, Sep. 2009.

[13] F. Henrotte, H. Heumann, E. Lange, and K. Hameyer, "Upwind 3-D vector potential formulation for electromagnetic braking simulations," *IEEE Trans. Magn*., vol. 46, no. 8, pp. 2835–2838,Aug. 2010.

[14] A. C. Smith, S. Williamson, A. Benhama, L. Counter, and J. M. Papadopoulos, "Magnetic drive couplings," in *Proc. IEE 9th EMD,* Canterbury, U.K., Sep. 1-3, 1999, pp. 232-236.

[15] A. Canova, and B. Vusini, "Analytical modeling of rotating eddy-current couplers," *IEEE Trans. Magn.,* vol. 41, no. 1, pp. 24-35, Jan. 2005.

[16] N. Paudel, and J. Z. Bird, "General 2-D steady-state force and power equations for a traveling time-varying magnetic source above a conductive plate," *IEEE Trans. Magn*., vol. 48, no. 1, pp. 95–100, Jan. 2012.

[17] J. Y. Choi and S. M. Jang, "Analytical magnetic torque calculations and experimental testing of radial flux permanent magnet-type eddy current brakes," *J. Appl. Phys.,* vol.111, no.7, pp. 07E712-07E712-3, Apr. 2012.

[18] H. J. Shin, J. Y. Choi, H. W. Cho, and S. M. Jang, "Analytical torque calculation and experimental testing of permanent magnet axial eddy current brake," *IEEE Trans. Magn.*, vol. 49, no. 7, pp. 4152–4155, Jul. 2013.

[19] S. Mohammadi, M. Mirsalim, and S. Vaez-Zadeh, "Non-linear modeling of eddy-current couplers," *IEEE Trans. Energy Convers.*, vol. 29, no. 1, pp. 224–231, Mar. 2014.

[20] J. Wang, H. Lin, S. Fang, and Y. Huang, "A general analytical model of permanent magnet eddy current couplings," *IEEE Trans. Magn.*, vol. 50, no. 1, p. 8 000 109, Jan. 2014.

[21] S. Mohammadi, and M. Mirsalim, "Design Optimization of Double-Sided Permanent-Magnet Radial-Flux Eddy-Current Couplers," *Electr. Power Sys. Res.*, vol. 108, pp. 282-292, Mar. 2014.

[22] R. L. Russell and K. H. Norsworthy, "Eddy currents and wall losses in screened-rotor induction motors," *Proc. Inst. Elect. Eng.*, vol. 105, no. 20, pp. 163- 175, Apr. 1958.

[23] K. J. W. Pluk, T. A. van Beek, J. W. Jansen, E. A. Lomonova, "Modeling and measurements on a finite rectangular conducting plate in an eddy –current damper," *IEEE Trans. Ind. Electron.*, vol. 61, no. 8, pp. 4061–4072, Aug. 2014.

[24] H. Zhang, B. Kou, Y. Jin, L. Zhang, H. Zhang, and L. Li, "Modeling and analysis of a novel planar eddy current damper," *J. Appl. Phys.,* vol. 115, 17E709 ,Jan. 2014.

[25] S. Paul, W. Bomela, N. Paudel, and J. Z. Bird, "3-D eddy-current torque modeling," *IEEE Trans. Magn.,* vol.50, no.2, p. 7022404, Feb. 2014.

[26] K. R. Shao, and J. D. Lavers, "Method of fundamental solutions based on the second order vector potential formulation for 3D eddy current analysis," *IEEE Trans. Magn.,* vol.29, no.6, pp. 2431-2433, Nov. 1993.

[27] K. J. Meessen, B. L. J. Gysen, J. J. H. Paulides, and E. A. Lomonova, "General formulation of fringing fields in 3-D cylindrical structures using Fourier analysis," *IEEE Trans. Magn.,* vol. 48, no. 8, pp. 2307-2323, Aug. 2012.

[28] O. de la Barrière, S. Hlioui, H. Ben Ahmed, M. Gabsi, and M. LoBue, "3-D formal resolution of Maxwell equations for the computation of the no-load flux in an axial flux permanent-magnet synchronous machine," *IEEE Trans. Magn*., vol. 48, no. 1, pp. 128–136, Jan. 2012.

[29] K. J. Meessen, J. J. H. Paulides, and E. A. Lomonova, "Force calculation in 3-D cylindrical structure using Fourier analysis and the Maxwell stress tensor," *IEEE Trans. Magn.,* vol. 49, no. 1, pp. 536-545, Jan. 2013.

[30] B. Dolisy, S. Mezani, T. Lubin, and J. Lévêque, "A new analytical torque formula for axial field permanent magnets coupling," *IEEE Trans. Energy Convers.*, to be published.

[31] Y. Marechal, and G. Meunier, "Computation of 2D and 3D eddy currents in moving conductors of electromagnetic retarders," *IEEE Trans. Magn.,* vol. 26, no. 5, pp. 2382-2384, Sep. 1990.